Physics of Fluids

RESEARCH ARTICLE | MARCH 13 2024

Flow dynamics of a liquid–liquid bi-swirl injector

Vishnu Natarajan ; Umesh Unnikrishnan ; Jeong-Yeol Choi ; Vigor Yang

Physics of Fluids 36, 032122 (2024)
https://doi.org/10.1063/5.0191490

Physics of Fluids ARTICLE pubs.aip.org/aip/pof

Flow dynamics of a liquid–liquid bi-swirl injector

Cite as: Phys. Fluids **36**, 032122 (2024); doi: 10.1063/5.0191490
Submitted: 14 December 2023 · Accepted: 25 February 2024 ·
Published Online: 13 March 2024

View Online Export Citation CrossMark

Vishnu Natarajan,[1] Umesh Unnikrishnan,[2] Jeong-Yeol Choi,[1,a)] and Vigor Yang[2]

AFFILIATIONS

[1]Department of Aerospace Engineering, Pusan National University, Busan 46241, South Korea
[2]School of Aerospace Engineering, Georgia Institute of Technology, Atlanta, Georgia 30332, USA

[a)]Author to whom correspondence should be addressed: aerochoi@pusan.ac.kr

ABSTRACT

This work presents detailed two-phase flow simulations of liquid–liquid bi-swirl injectors for engineering applications. Liquid oxygen and kerosene are delivered into the injector, which is initially filled with air. A parametric study is conducted on the recess length of the inner tube to investigate its effect on the flow dynamics and spray pattern. The simulations are performed using an improved multiphase flow solver in OpenFOAM, which employs the volume-of-fluid approach for interface tracking and the large-eddy simulation technique for turbulence modeling. Detailed flow dynamics of both fuel and oxidizer, along with their spray patterns, are examined systematically. A comprehensive account is provided on the impact of the recess length on flow evolution, including the film thickness, air core diameter, and spray cone angle. Spectral and dynamic mode decomposition analyses are performed to further examine the flow structures and dynamics. Results from this study can be effectively used to facilitate the design optimization of injectors for liquid-fueled propulsion systems.

I. INTRODUCTION

Injector plays a crucial role in determining the characteristics of atomization, mixing, and combustion in a combustion device.[1,2] Over the years, various injector types have been developed to achieve efficient mixing of propellants, such as impinging-jet, pintle, shear, and swirl injectors.[1–4] Among these, coaxial injectors, which consist of an inner injector enveloped by a concentric outer injector, have emerged as a prominent feature due to their superior performance, stability, and versatility. Coaxial injectors have multifaceted benefits, including efficient atomization, homogenization of propellants, and a lower precision level required for manufacturing.[5] Coaxial injectors can be categorized based on the thermodynamic states of propellants, including gas–gas, gas–liquid, and liquid–liquid combinations. In scenarios where a storable liquid–liquid combination is utilized, swirl injectors are commonly implemented for both the inner and outer injectors to achieve optimal atomization and mixing.[6]

Liquid–liquid bi-swirl coaxial injectors comprise a pair of concentrically arranged swirl injectors, which facilitate effective atomization and mixing of propellants. Liquid–liquid bi-swirl coaxial injectors have proven particularly advantageous for liquid rocket engines (LREs) due to their high mixing efficiency within limited space.[7–9] The specific liquid–liquid bi-swirl injector examined in this study mimics the one utilized in the RD-0110 rocket engine,[10] as shown schematically in Fig. 1. A closed-type swirl injector[11] is used as the inner element for liquid oxygen, and an open-type injector[12] as the outer element for kerosene. Mixing of the two propellant streams occurs either inside or outside the injector, depending on the recess length of the inner element, which is defined as the distance between the exit of the inner element and the exit of the injector.

Extensive theoretical, experimental, and numerical studies have been conducted to investigate the dynamics of swirl injectors.[13,14] Detailed understanding of injector flow physics based on inviscid-flow theories was achieved for a wide range of injector geometries and operating conditions.[1,2] Sivakumar and Raghunandan[7–9] experimentally studied the effect of recess length on droplet size and found that atomization was adversely affected by the recess length. Liquid sheets merging and separating during hysteresis can cause a significant change in the spray characteristics, which in turn can have a significant impact on combustion dynamics.

Han *et al.*[15] utilized backlight stroboscopic photography to study the mixing characteristics of a bi-swirl injector with water and kerosene as the working fluids. It was found that the propellant mass distribution and mixing efficiency were significantly affected by the recess length and that there exists an optimal length for achieving maximum mixing efficiency. Kim *et al.*[6] carried out experiments on the effect of the recess length on the spray properties of a liquid–liquid bi-swirl injector. The spray cone and breakup length were examined, along with the spray patterns at the internal, exterior, and tip mixing conditions. Yoon and Ahn[16] studied the effect of the recess length, swirl direction, and mixture ratio on the spray cone angles of a bi-swirl injector.

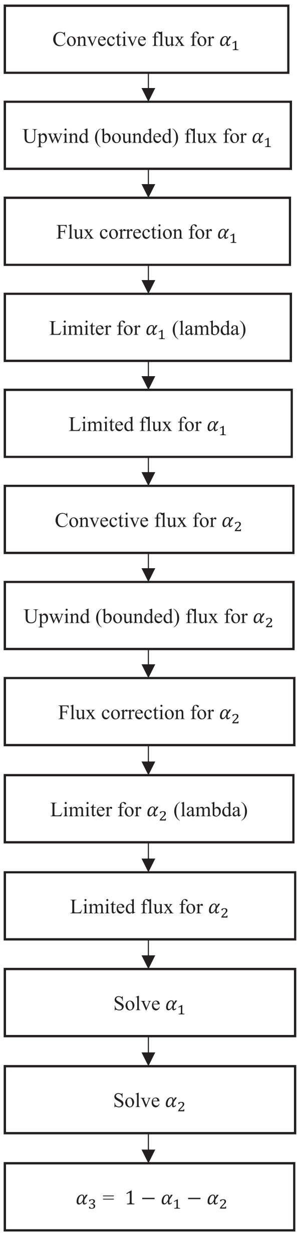

FIG. 1. Calculation procedure of fluid volume fraction α in the modified interMixingFoam solver.

A variety of mixture ratios were considered under three different mixing flow conditions.

In parallel to experimental efforts, Lee *et al.*[17] conducted a numerical study on the spray characteristics of a bi-swirl injector for various recess lengths. Although their numerical findings did not align with experimental results, a trend comparable to the actual data were obtained. Wang *et al.*[18] performed large-eddy simulations to analyze the fluid dynamics and mixing characteristics of a LOX/kerosene bi-swirl injector at supercritical conditions. Results provided detailed information about injector flow physics and design optimization. The study later was extended to investigate the near-field flame dynamics[19] and flame evolution[20] of LOX/kerosene bi-swirl injectors.

In spite of the progress made to date, intricate interfacial dynamics between injected fluids, as well as ensued atomization and breakup mechanisms, remain to be explored. Further, the flow evolution from individual injection orifices and subsequent interactions in the flow path need to be investigated. The literature in this area is sparse, with only a handful of numerical simulations available.[21–24] The present study performs multiphase flow simulations by means of a modified interMixingFoam solver in OpenFOAM. The purpose is to investigate the flow structures and dynamics of a liquid–liquid bi-swirl injector with different recess lengths. Detailed flow evolution within the injector and spray characteristics downstream of the injector are examined systematically. To focus on the fluid dynamics aspect without complications from the thermodynamic phase change, nonvolatile LOX and kerosene are employed as the working fluids. The findings shed light on the complex flow dynamics of liquid–liquid bi-swirl injectors and can be used to guide injector design and optimization.

II. NUMERICAL APPROACH

The numerical simulations in the present study are carried out using a modified interMixingFoam solver in the OpenFOAM CFD software. It is an updated version of the interFoam solver used in our previous work.[12] This solver is specifically designed to handle simulations of three different incompressible fluids, with two being liquids. The VOF phase-fraction-based interface capturing method is utilized to treat fluid interfacial dynamics. Turbulence closure is achieved using a large eddy simulation (LES) technique based on a one-equation eddy viscosity turbulence model.

A. Calculations of fluid volume fractions

Fluid volume fraction, denoted by α, is calculated using the interMixingFoam solver. Here α_1, α_2, and α_3 to represent the volume fractions of air, liquid oxygen (LOX), and kerosene, respectively. The sum of these three volume fractions equals unity given as

$$\alpha_1 + \alpha_2 + \alpha_3 = 1. \tag{1}$$

Figure 1 shows the calculation procedure of α. The volume fraction for each fluid is bounded and the values lie between 0 and 1. This prevents the occurrence of nonphysical solutions, which can lead to artificial smearing of the interface. The bounded upwind scheme effectively captures the interface by balancing the need for sharpness with the stability requirements of the numerical method. This is crucial in simulations involving complex interfacial dynamics.

The numerical approach involves the discretization of governing equations using the finite-volume method on an unstructured grid. A second-order implicit, bounded Crank–Nicolson scheme is utilized for time integration. Gauss linear interpolation is employed to compute gradients by interpolating values from cell centers to face centers. Divergence terms are treated by means of linear interpolation except for the divergence of φ (flux across cell faces) and α, for which the van Leer limiter is employed. The corrected scheme is used for the surface normal gradient. In spite of the low non-orthogonality of the grid, two nonorthogonal iterations were used in the simulations to obtain a satisfactory balance between computational efficiency and solution accuracy. For LES, the zero-gradient conditions are set for nut and inletOutlet, and a uniform value of 10^{-5} is used for k. The smooth delta filter is used for the LES within which the delta type is cubeRootVol with deltaCoeff of 1.0 and maxDeltaRatio of 1.1. The value of Ck is 0.094. The mass and momentum conservation equations are calculated using the PISO algorithm. The pressure term is solved using a preconditioned conjugate gradient solver with the diagonal incomplete-Cholesky preconditioner, and a smooth solver with the Gauss–Seidel smoother was employed to solve all other terms. The error tolerance is set to 10^{-8} and the relative tolerance is set to 0. This means that the iterations would continue until the absolute error in the solution falls below 10^{-8}. The average number of iterations for solving the pressure field is approximately 650. The present numerical approach is expected to yield reliable results for the flow physics under consideration.

B. Injector configuration and boundary conditions

Figure 2 shows the bi-swirl injector considered in the present study, mimicking the injector utilized in the RD-0110 engine.[8] The configuration comprises an inner closed-type injector and an outer open-type injector arranged concentrically. Each injector has six tangential inlets for propellant delivery. The length of the entire injector is 24.2 mm and the exit diameter is 10 mm. The outer injector element is 10.5 mm in length, with an outer diameter of 10 mm and a width of 1.5 mm. The tangential inlets in the outer and inner injector elements are cylindrical, with a length of 5 mm, and diameters of 0.7 and 1.7 mm, respectively. Each tangential inlet for the outer and inner injectors is fixed at 4.5 and 3.5 mm from the center, respectively. The inner injector element consists of a swirl chamber, a converging section, and an exit. The swirl chamber is 10.4 mm long, with a diameter of 9 mm, and the orifice section has a diameter of 7 mm, which is connected via a convergent section. The recess length L of the inner injector element is defined as the distance between the exits of the inner and outer injector elements. In the current study, three different recess lengths of 1.5, 2.5, and 5 mm are considered to explore the flow behaviors under different mixing conditions.[10] To investigate the liquid breakup characteristics and spray pattern downstream of the injector, an external domain measuring 35 mm in length and 30 mm in diameter is included as part of the computational domain. The initial and boundary conditions are obtained from Rubinsky[10] and listed in Table I. The ambient pressure is set to 1 bar.

The computational grid system employs an unstructured grid comprising tetrahedral cells, as depicted in Fig. 3. The head of the inner injector is zoomed to show the grids in the tangential inlets. The very-fine mesh case comprises a total of 6 995 692 nodes, with cells sized between 100 and 200 μm throughout the computational domain. The smallest cells are primarily used in the injection orifices and near the injector walls. The larger cells are mostly for the exterior domain. The total number of cells for the very-fine mesh case is 39 772 732. The maximum Courant number is set at 0.5 to ensure numerical stability. The computational domain is divided into 552 subdomains using the Scotch decomposition method in OpenFOAM, and the decomposed domain is then computed using MPI. The simulation is performed for a certain period of time to ensure that the flowfield develops completely and reaches a fully stationary state.

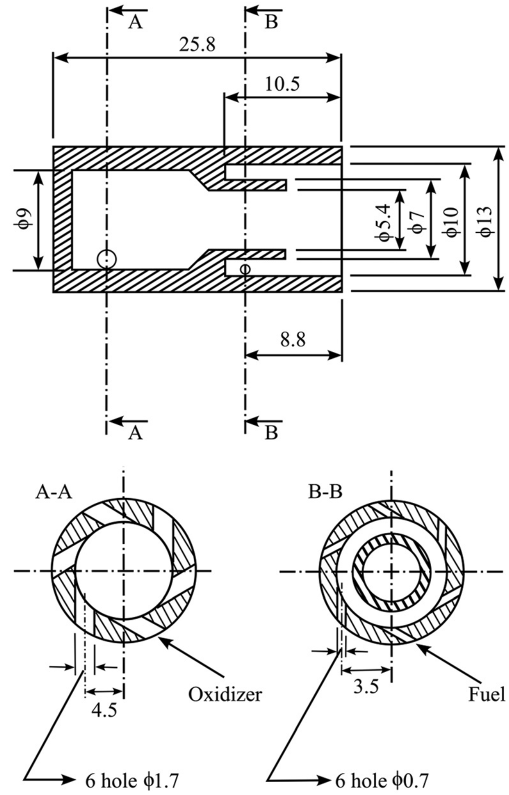

FIG. 2. Schematic of the bi-swirl injector configuration.

TABLE I. Inflow conditions.

	Oxidizer	Fuel
Fluid	Nonvolatile LOX	Kerosene
Mass flow rate (g/s)	172.90	64.80
Pressure drop, ΔP (bar)	4.26	6.96
Density (kg/m^3)	1141	810

C. Model validation and grid refinement study

To validate the modified interMixingFoam solver, we adopt a classical problem of single droplet impingement due to its multifaceted splashing event. The experimental result of Cossali *et al.*[25] was used for validation. The Weber number We of 667 and dimensionless droplet diameter δ of 0.67 were selected, corresponding to the droplet diameter of 3.82 mm and liquid film thickness of 2.56 mm, respectively. To assess the fidelity of our results, attention is given to the solver's prediction of the inner crown diameter (D_{in}) against experimental measurements, as shown in Fig. 4. The comparison established the solver's capability to predict the underlying physics of complex phenomena. To further validate the accuracy of the solver, the calculated spray cone angles of 124° and 76° for the inner and outer injector, respectively, were compared to the values of 135° and 80° reported in the literature[10] for the outer open-type

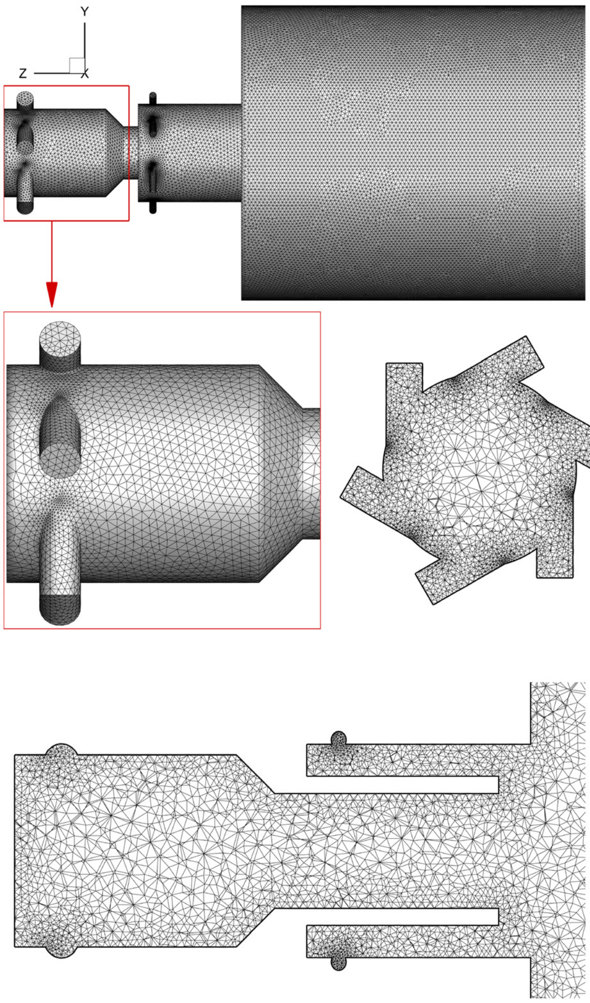

FIG. 3. Computational grid and the oxidizer inlet parts zoomed in for clarity (coarse mesh is shown for clarity).

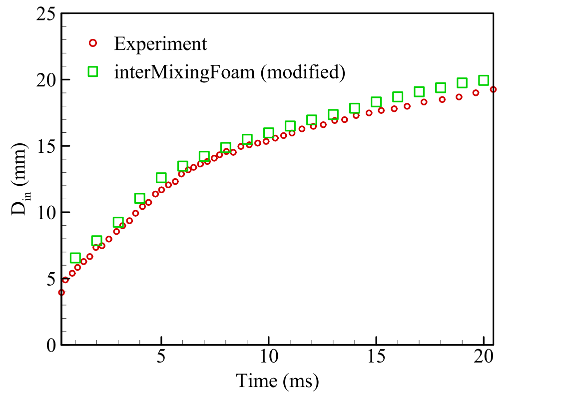

FIG. 4. Comparison of obtained results with experimental results of Cossali *et al.*[25]

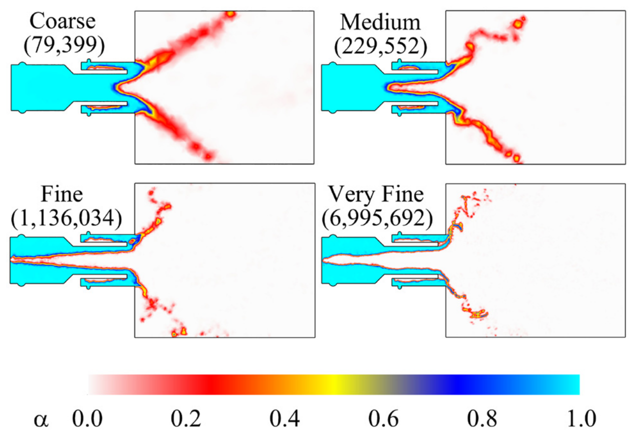

FIG. 5. Liquid volume fractions for various grid resolutions.

injector and inner closed-type injector, respectively. Reasonable agreement was achieved, further justifying the relevance of the solver in the present study.

A grid refinement study is carried out by using four different mesh resolutions, referred to as coarse, medium, fine, and very-fine meshes. Figure 5 shows the distributions of liquid volume fractions for the four different meshes. For coarse mesh, even the air core development is not captured due to the smearing of the interface. In the medium mesh case, a small air core is seen while in the fine mesh case, a fully developed air core is clearly visible. The interface is more distinct and the interactions of the spray jets originating from the inner and outer injectors are clearly observed as the grid resolution is increased. Figure 6 shows the pressure profiles in the radial direction at the injector exit for different mesh resolutions. Even though the profiles with fine and very-fine meshes are practically identical, the rest of the study will focus on results obtained using very-fine meshes to provide high-resolution flow physics over a wide range of scales.

III. RESULTS AND DISCUSSION

A. Flowfield development

1. Recess length (L = 1.5 mm)

Figure 7 shows the volume-fraction field of air for the bi-swirl injector with a recess length of 1.5 mm. The spatiotemporal evolution of the liquid flow is clearly observed. The liquid streams originating from the inner and outer injector elements meet downstream of the bi-swirl injector exit, a situation commonly referred to as external mixing. The injected fuel and oxidizer enter the swirl chamber after being injected in through the six tangential inlets. The flow in the inner injector element reaches the converged portion at about t = 1.6 ms and is reflected at t = 2.0 ms. The liquid flow exits the injector at t = 4.2 ms. Since there is no converging section in the outer injector element, the injected liquid kerosene travels through the injector quickly and reaches the exit at 1.6 ms. The spray produced downstream of the bi-swirl injector at early times solely originates from the outer injector element. Even after the spray from the inner injector element reaches the exit of the bi-swirl injector at around t = 4.0 ms, the two sprays develop separately for some time. There is a time delay of about 1.0–1.5 ms for the two sprays to intercept each other. The outer spray initially has a

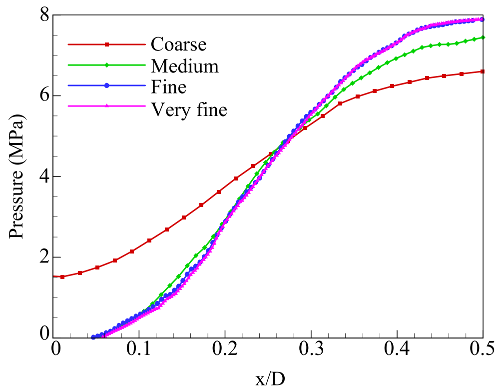

FIG. 6. Pressure profile in the radial location at the injector exit for L = 1.5 mm.

wider spray cone angle. After the inner liquid stream reaches the injector exit and merges with the outer spray, the combined spray cone angle changes and decreases slightly from the original outer spray angle. Unsteady merging and separation of the two sprays occur, rendering a continuous oscillation of the spray cone angle with time. The inner and outer injector elements both exhibit a modest increase in film thickness after the two liquid sprays collide. As a result, the void region in the outer injector slightly reduces its volume, as shown in Fig. 7. When the two sprays collide, the contact region acts as a local stagnation region, leading to a slight increase in the liquid film thickness with a reduced void region. Figure 8 shows the flow development from the fuel and oxidizer injection orifices. The spatiotemporal evolution of the flowfield is clearly observed.

2. Recess length (L = 2.5 mm)

Figure 9 shows the volume-fraction field of air for the bi-swirl injector with a recess length of 2.5 mm. The sprays from the inner and outer injector elements meet at the edge of the bi-swirl injector, a situation referred to as tip mixing. The initial development of the flowfield inside both injector elements is mostly similar to the case of external mixing. The increase in the recess length leads to a reduced length of the inner injector element. The liquid flow reaches the exit of the inner injector element a little before 4.0 ms, compared to the case of L = 1.5 mm. The intersection of the two sprays is thus advanced to around t = 4.6 ms. The flowfield of the outer injector element is observed to be greatly affected by the

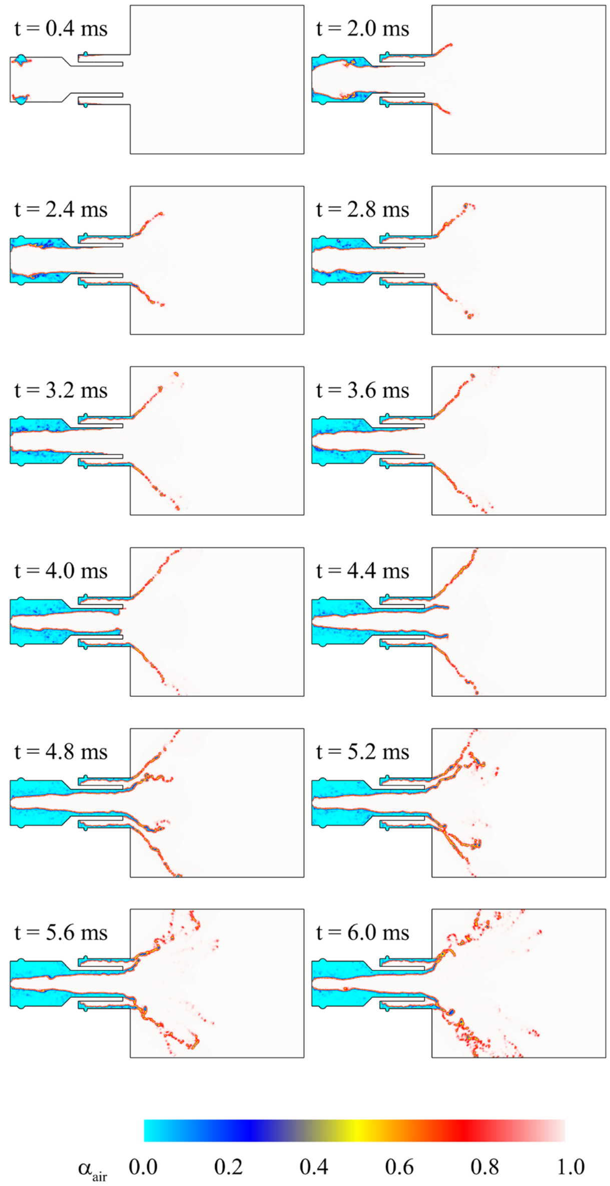

FIG. 7. Air volume-fraction field showing the flow development in the bi-swirl injector for a recess length of 1.5 mm.

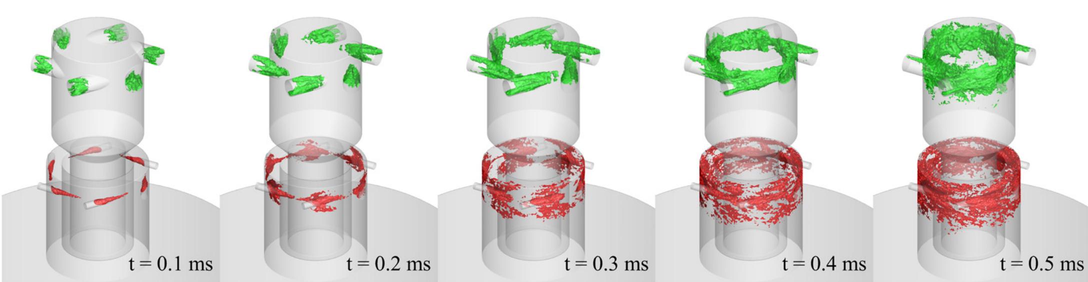

FIG. 8. Flowfield development from the injection orifices for the bi-swirl injector.

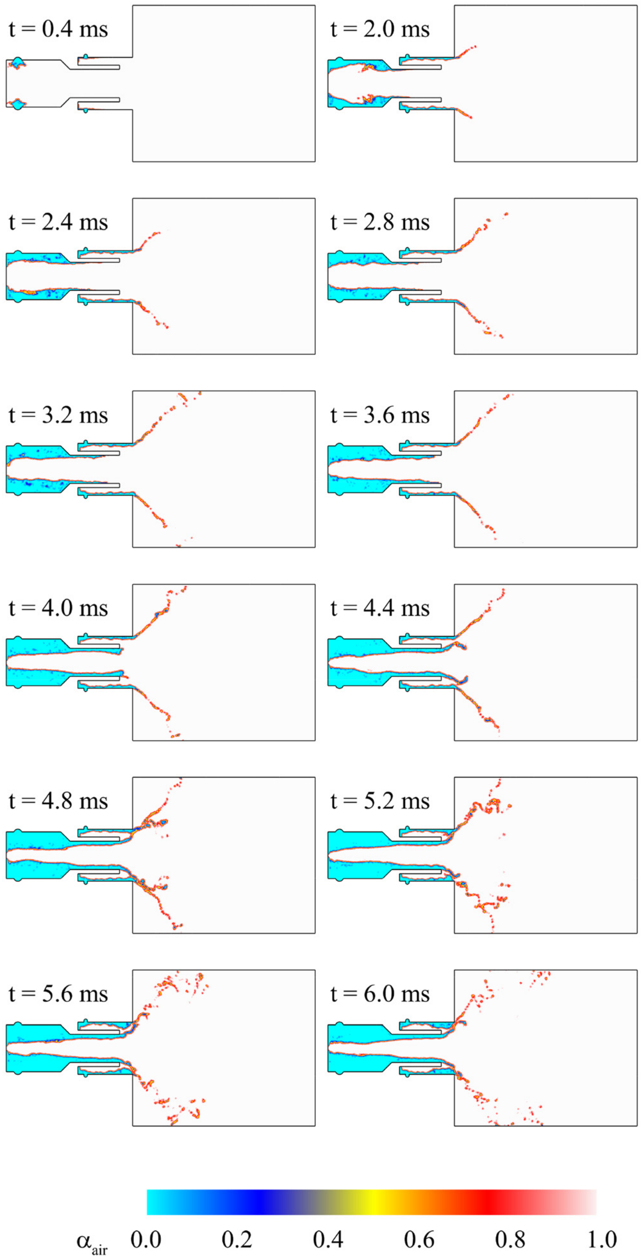

FIG. 9. Air volume-fraction field showing the flow development in the bi-swirl injector for a recess length of 2.5 mm.

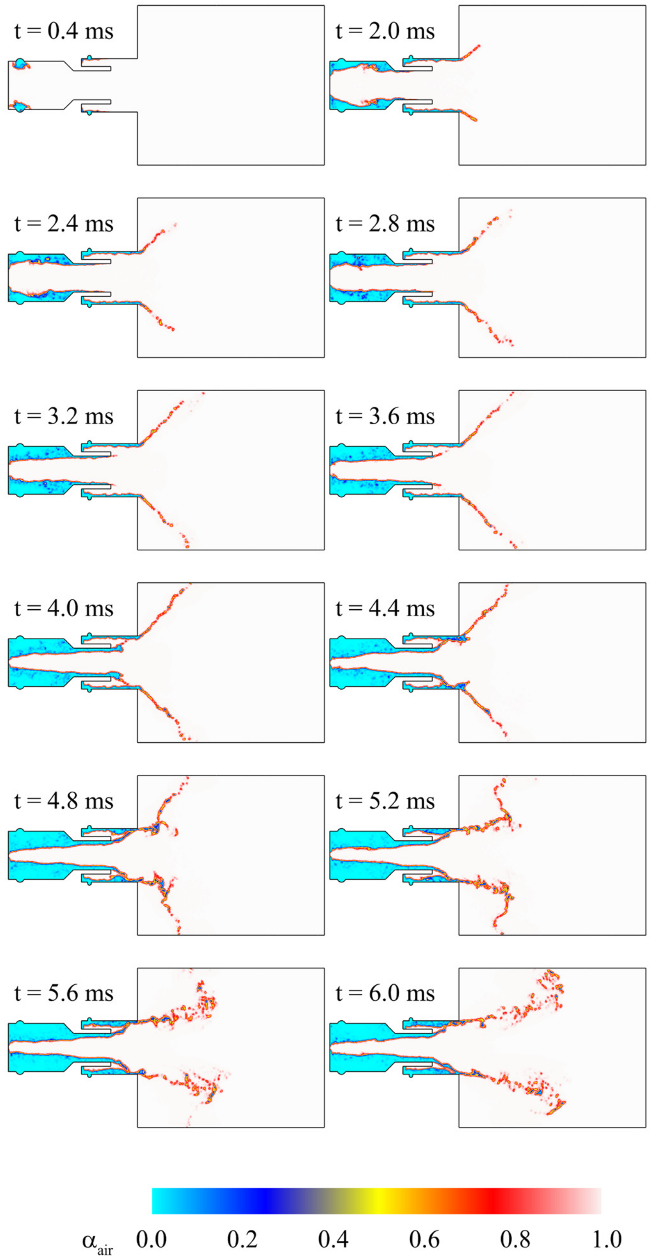

FIG. 10. Air volume-fraction field showing the flow development in the bi-swirl injector for a recess length of 5.0 mm.

intersection of the two sprays. The increase in the liquid film thickness of the outer injector element, due to the intersection of the two sprays, is considerably larger than its counterpart with a recess length of 1.5 mm. A local stagnation region occurs in the outer injector element due to the interception of the two sprays at the edge of the injector exit. It then causes the film thickness to increase with reduced air volume. Figure 8 also indicates the oscillation of spray intersection around the outer injector exit.

3. Recess length (L = 5.0 mm)

Figure 10 shows the spatiotemporal evolution of the injector flow in the case of an extended recess length of 5.0 mm. Internal mixing takes place, where the inner and outer sprays intersect and mix inside the bi-swirl injector. The higher recess length in this case leads to a shorter inner injector element. The injected liquid reaches the exit of the inner injector element at around t = 3.6 ms, which is earlier than in

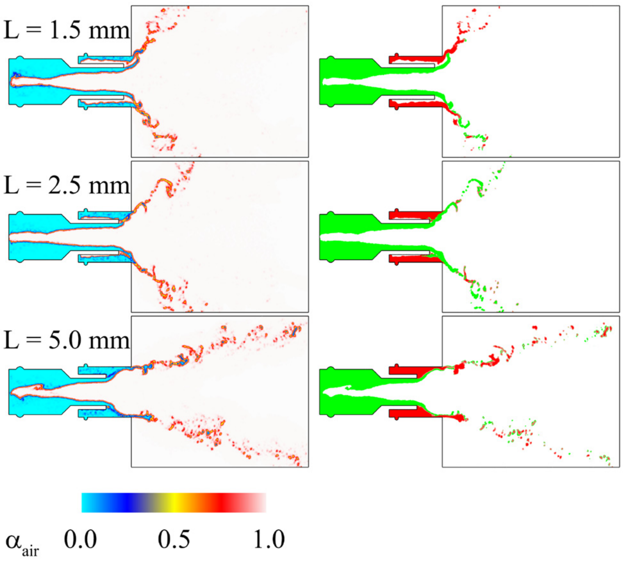

FIG. 11. Distributions of air volume fraction in the bi-swirl injector with three different recess lengths at t = 10 ms.

the previous cases. The liquid flow from the inner injector element directly impinges onto the outer injector flow without much time delay inside the injector itself. Such interaction helps block the outer injector flow and creates a stagnation region which substantially increases the film thickness. The flow passage in the outer injector element is fully occupied by liquid kerosene. The mixing of the two liquid streams also proceeds at a faster rate. The spray pattern initially formed in the external region solely by the outer injector element completely changes when the two sprays intersect and merge. The merged stream continues to swirl while convecting through the injector. The resultant spray has a considerably smaller cone angle compared to the initial angle formed by the outer spray. The transition of the cone angle begins upon coalescence of the two sprays from the injector exit and gradually propagates downstream with time.

B. Internal flowfield

Figure 11 shows the volume-fraction distributions of air, oxidizer, and fuel for the bi-swirl injector with three different recess lengths of 1.5, 2.5, and 5 mm, at t = 10 ms. The corresponding modes of external, tip, and internal mixing are clearly observed. The flow phenomena are further substantiated by Fig. 12, showing the distributions of air volume fraction on the cross sections at the injector and the inner injector element exits. The liquid interface is wavy along the streamwise direction, and a helical flow path is observed inside the injector. Uneven variation in the liquid film thickness occurs. An air core forms when the centrifugal force predominates the viscous force. Under this situation, an air core is established inside the inner injector, and a void region is found in the outer annulus. With an increase in recess length, the thickness of the liquid film in the outer annulus increases, and the void region shrinks. For the internal mixing case (L = 5 mm), the void region disappears, and liquid kerosene occupies the entire flow path in the outer annulus. For the tip mixing case (L = 2.5 mm), intermittent air pockets are seen. For the external mixing case (L = 1.5 mm), two

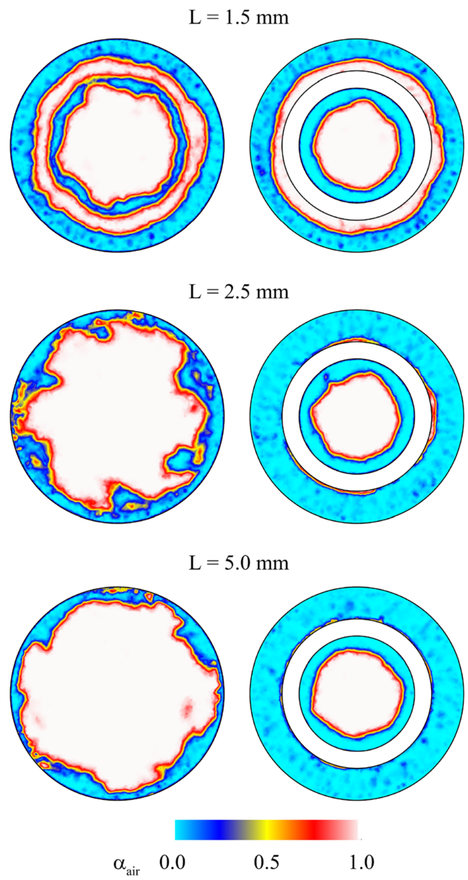

FIG. 12. Distributions of air volume fraction at bi-injector exit (left) and inner injector exit (right) for different recess lengths at t = 10 ms.

separate quasi-circular liquid streams take place at the exit of the injector, and mixing occurs further downstream. In the internal mixing case, the outer annulus is fully filled with fuel, while in the tip mixing case, it is nearly filled with a minimal gap. Conversely, the external mixing case exhibits a distinct gap, lacking thermal protection during combustion. The liquid film thickness at the injector exit is measured by taking the temporal and spatial averaging in the circumferential direction. For a recess length of 1.5 mm (external mixing), the inner and outer film thicknesses of 0.78 and 0.93 mm are obtained. The film thickness measures 0.82 mm for a recess length of 2.5 mm (tip mixing). The film thickness further decreases to 0.55 mm for a recess length of 5.0 mm (internal mixing). This result clearly indicates a trend that as the recess length of the inner injector element increases, the liquid film thickness decreases. The pivotal role of recess length in shaping the characteristics of the liquid film and subsequent atomization is firmly established.

C. External spray field

Figure 13 presents the spray fields for kerosene and LOX, as well as their combined spray field for different recess lengths. The isosurfaces of the volume fraction $\alpha = 0.25$ are presented for both

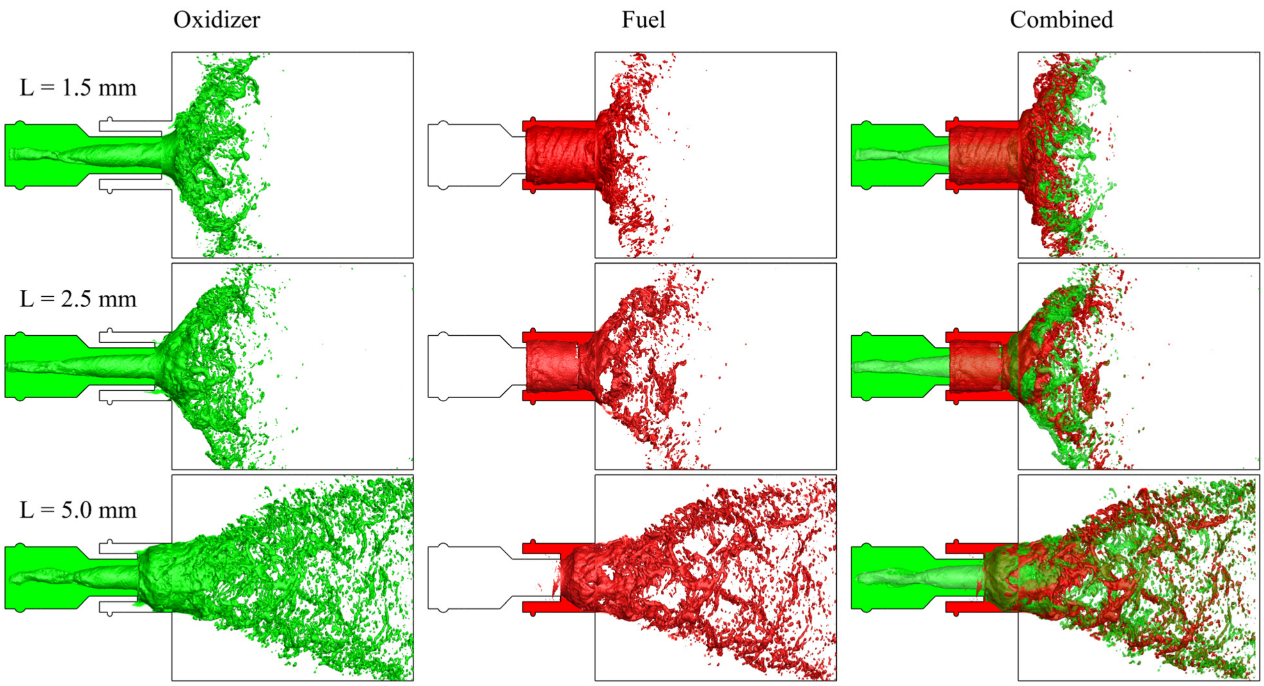

FIG. 13. Iso-surfaces of $\alpha = 0.25$ for fuel and oxidizer with different recess lengths at t = 10 ms.

kerosene (red) and LOX (green). A conical spray pattern forms downstream of the injector, and the spray cone angle decreases with increasing recess length. This trend agrees with the experimental observations by Kim *et al.*[6] For the case of external mixing, the spray cone closely follows the trend of the outer liquid film, yielding a diffuse jet with a larger spray cone angle. The inner liquid film has a larger spreading angle to facilitate the merging of the outer and inner liquid films downstream of the injector exit. For the internal mixing case, however, the two liquid films meet within the injector. This provides sufficient passage length for the two liquid films to interact within the confines of the injector, producing a more homogeneous mixture and a smaller cone of the resultant spray. The spray cone angles have the values of 136°, 118°, and 59° for the recess lengths of 1.5, 2.5, and 5.0 mm, respectively. The spray cone angle decreases with increasing recess length.

Observations are made of liquid surface instability waves within the injector elements, which manifest in the sinuous and varicose modes. These waves lead to the stretching and eventual breakdown of the liquid film into ligaments, a process that occurs at the wave antinodes. The liquid sheet breaks down after exiting the injector when the inertial force overrides the viscous force and surface tension. The growth of the instability waves inside the injector is the primary cause of the liquid sheet breakup.

D. Streamlines

Figure 14 shows the distributions of air volume fraction on various cross sections inside the injector, accompanied by two streamlines—one originating from the inner injector element and the other from the outer annulus. These streamlines provide valuable insights into the flow behaviors as they travel within the injector. The swirling motion persists near the convergent section for an extended duration, followed by acceleration as it passes through the orifice. Conversely, in the outer annulus, the swirling flow exhibits a smoother initial motion

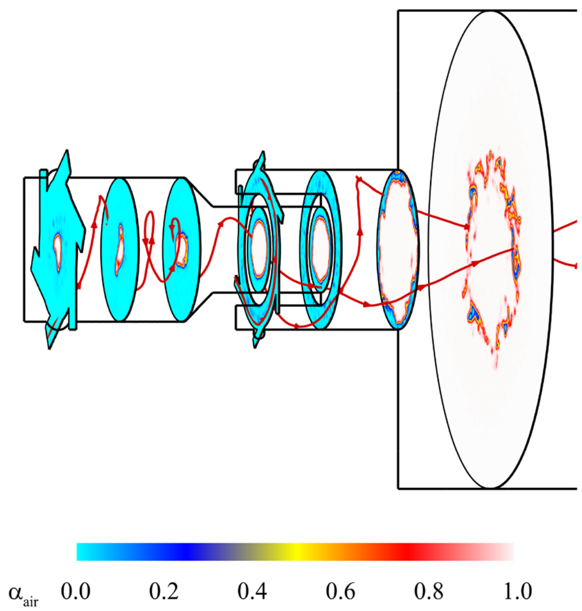

FIG. 14. Distributions of air volume fraction on different cross sections inside bi-swirl injector with recess length L = 5.0 mm at t = 10 ms and two streamlines originating from outer and inner injectors.

until the point of interaction between the two liquid sprays. Notably, the convergence of these two streams significantly alters the streamline in the outer injector element, as evidenced in Fig. 14. This alteration is characterized by a slight increase in the axial velocity of the outer injector flow due to the merging of the two liquid streams.

E. Temporal evolution of flowfield

Figure 15 presents the temporal evolution of the flowfield near the injector exit, showcasing the dynamic interplay between the kerosene and LOX streams for different recess lengths. Velocity vectors are superimposed on these contours to provide a more comprehensive understanding of the flowfield.

Figure 16 shows the temporal evolution of iso-surface contours of fuel and oxidizer at the volume fraction of $\alpha = 0.25$. The dynamics of surface waves are crucial in shaping the properties of the liquid film and subsequent atomization process. These surface waves introduce instabilities in the liquid film, causing fluctuations in its thickness and then leading to its breakup and atomization. The surface waves consist of two primary modes: sinuous and varicose. The sinuous mode drives the amplification of instability waves within the liquid film, while the varicose mode plays a pivotal role in the actual fragmentation of the liquid film. The air core, if designed properly, may serve as a damper to mitigate pressure fluctuations originating from the combustion chamber. The variation of the spray cone geometry over time is clearly visible, providing insights into how this critical parameter evolves during the course of the injection process. These observations collectively offer a comprehensive insight into the dynamics of the air core, liquid stream, and associated phenomena within the bi-swirl injector.

F. Vorticity dynamics

Figure 17 shows the vorticity fields in the injectors with different recess lengths. All three vorticity components are presented. For the x-component of vorticity, it is observed that positive values are concentrated on the inner side of the swirling flow in the lower section, while negative values predominate in the upper section. This structure emerges because the flow exhibits positive axial swirling in the lower half and negative axial swirling in the upper half. Interestingly, the value of x-component vorticity is reversed on the outer surface of the liquid spray. Within the region where LOX and kerosene intersect inside the injector, the x-component of vorticity remains negative in the lower part and positive in the upper part. Consequently, the direction of spin of the x-component of vorticity on the outer and inner sides of the swirl flow are opposite to each other. The y-component of vorticity has distributions of positive and negative values in the top and bottom parts of the injector. This variation signifies different rotational directions relative to the center axis. Finally, the z-component of vorticity has positive values in the central region of the injector, where the interface between air and liquid is situated.

Figure 18 shows the distributions of vorticity magnitude in the injectors with three different recess lengths. The vorticity magnitude is significantly higher along the injector surface and liquid/air interface. In the spray region, the intricate structure of vorticity becomes readily

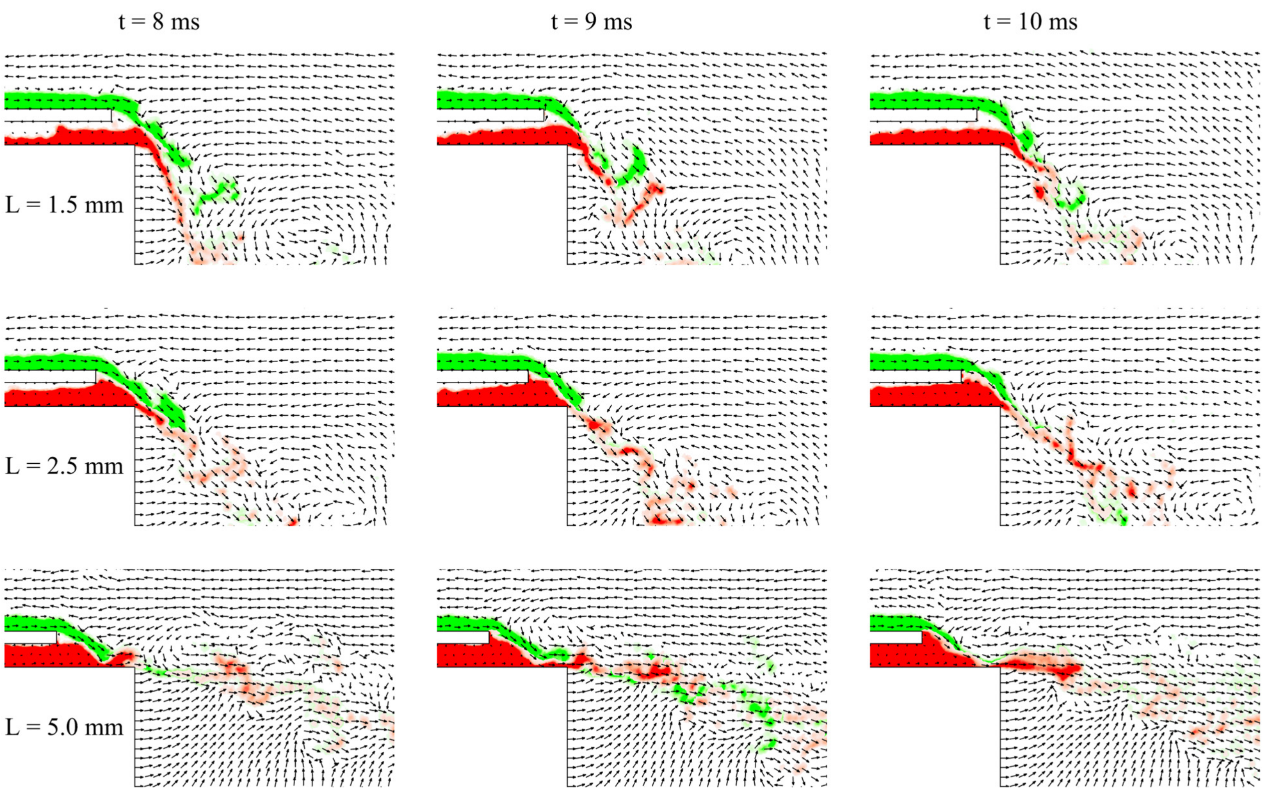

FIG. 15. Temporal evolution of flowfield near the bi-swirl injector exit with different recess lengths.

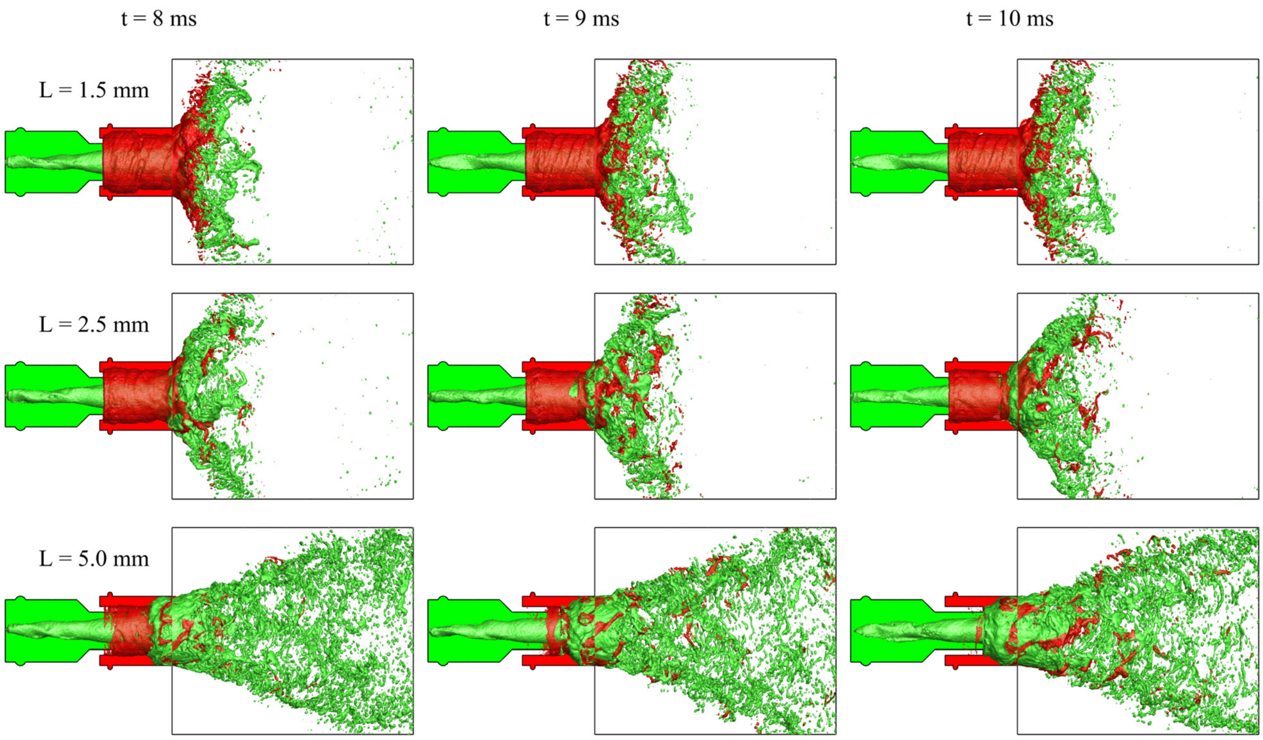

FIG. 16. Temporal evolution of iso-surface contours of fuel and oxidizer at $\alpha = 0.25$ for the bi-swirl injector with different recess lengths.

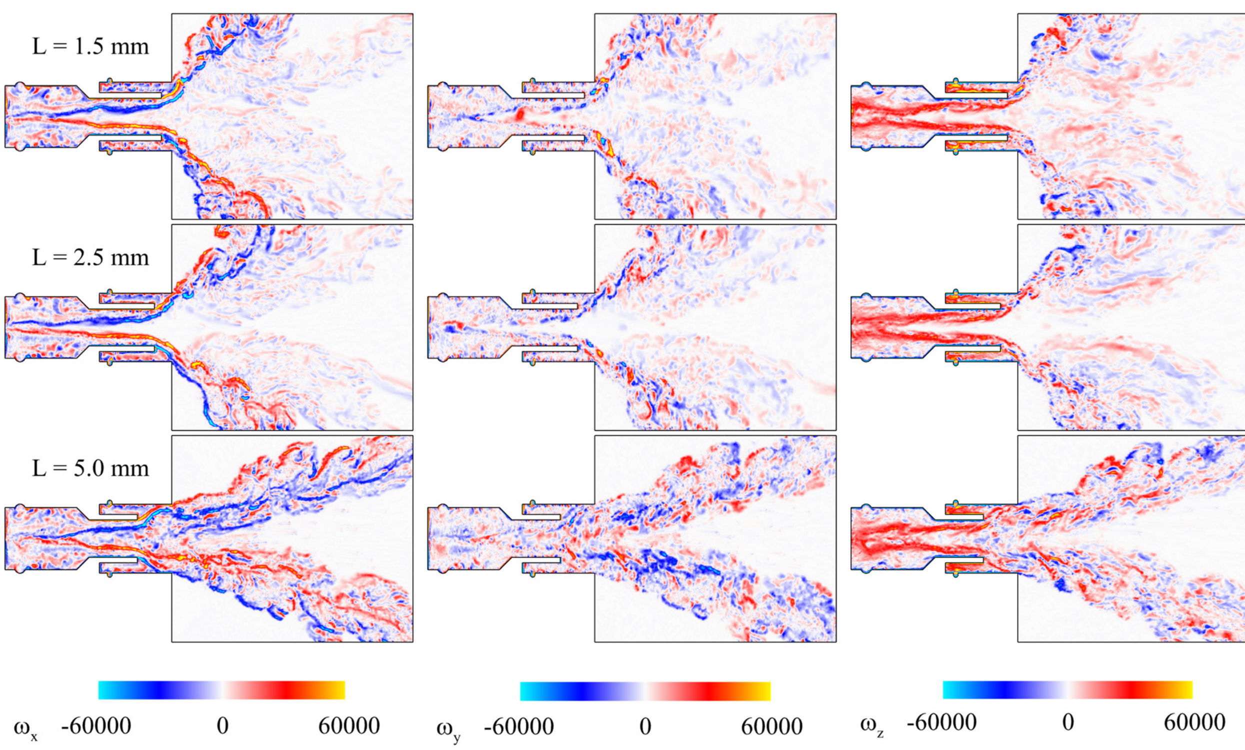

FIG. 17. Vorticity fields in the bi-swirl injector with various recess lengths.

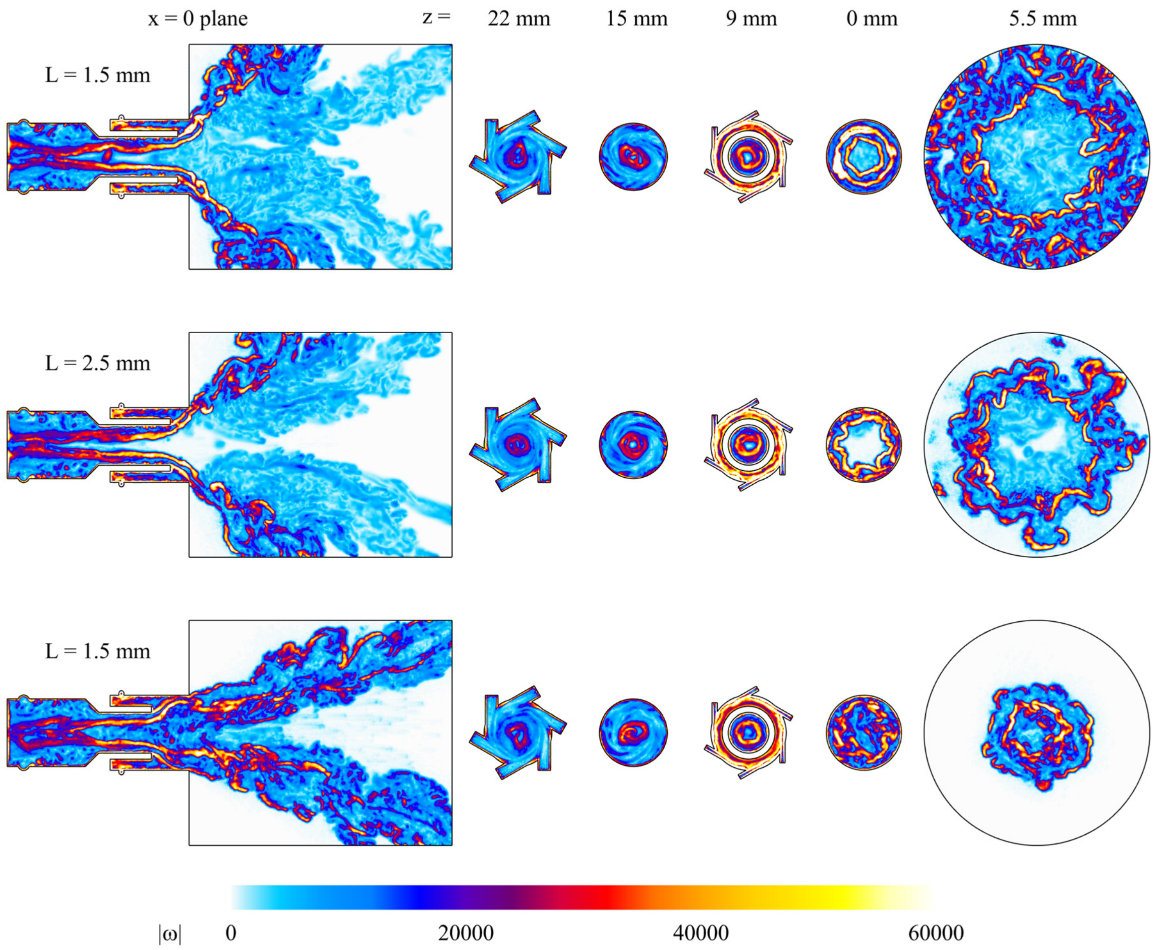

FIG. 18. Vorticity magnitude for a bi-swirl injector with different recess lengths.

apparent. Vortex stretching becomes prominent downstream of the injector. This process serves as a fundamental mechanism through which turbulent energy is transferred to smaller scales within the flow.

G. Spectral analysis

Spectral analysis is performed to quantify the injector flow dynamics. Table II lists the probe locations where the location (0, 0, 0) denotes the center of the injector exit plane. The data are collected over a time window of t = 0.7–10 ms. The sampling time interval is 1×10^{-7} s.

Figure 19 presents the spectral analysis of pressure fluctuations at various circumferential locations. For a recess length of L = 1.5 mm, the power spectral density (PSD) exhibits peak values between frequencies of 1.1 and 4.0 kHz. Specifically, probe 2 shows the highest peak at the frequency of 4.0 kHz, whereas probe 1 demonstrates the lowest peak at around 1.1 kHz. With a recess length of L = 2.5 mm, the PSD peaks are observed within the frequency range of 2.0–8.1 kHz. In this case, probe 3 displays the highest peak at 8.1 kHz, while the lowest peak appears at probe 1 with a frequency around 2.0 kHz. For the recess length of L = 5.0 mm, the PSD peaks are observed in the frequency range of 3.2–9.5 kHz. The highest peak occurs at probe 3 with a frequency of 9.5 kHz, whereas probe 2 exhibits the lowest peak at 3.2 kHz. The PSD values exhibit an increase with increasing recess length and then a decrease for the internal mixing case.

Figure 20 presents the spectral analysis of pressure fluctuation at various longitudinal locations where the two liquid flows meet. For a

TABLE II. Probe locations for spectral analysis.

Probe	Location (x, y, z), mm
1	(4.75, 0, 0)
2	(0, 4.75, 0)
3	(−4.75, 0, 0)
4	(0, −4.75, 0)
5	(4.75, 0, 1)
6	(4.75, 0, 2)
7	(4.75, 0, 3)
8	(4.75, 0, 4)

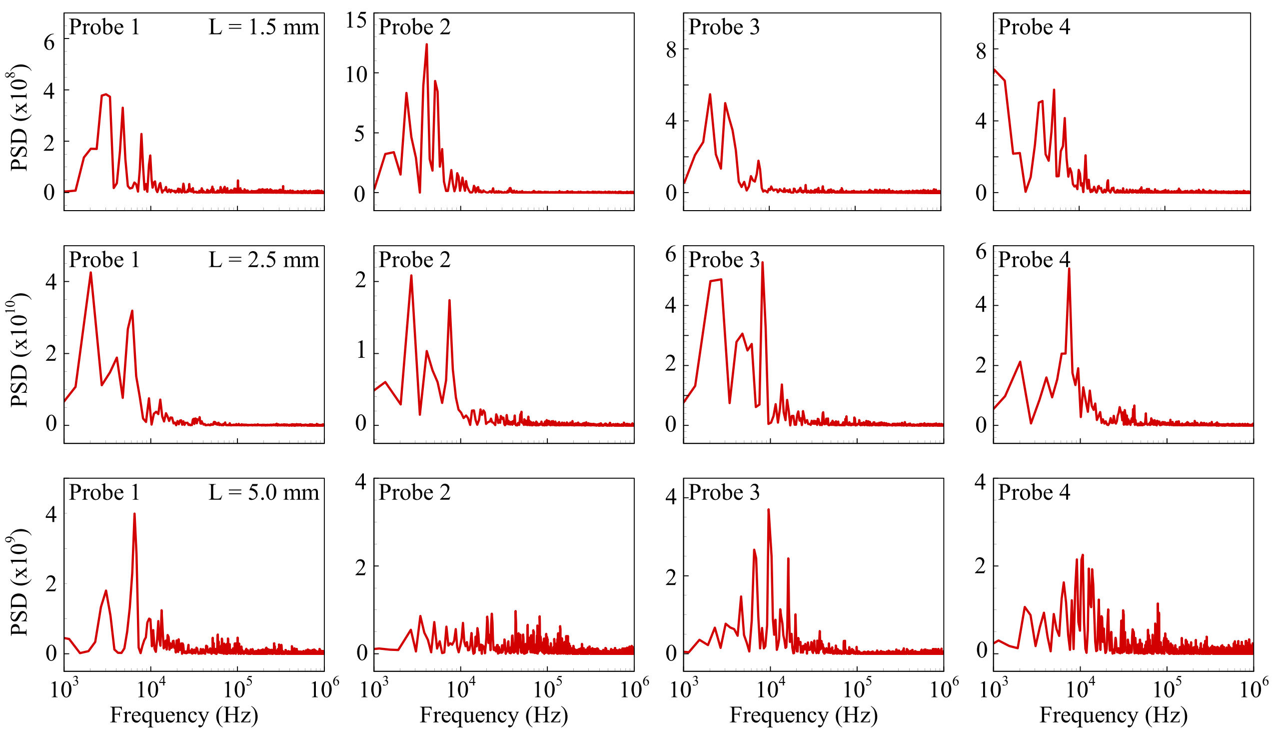

FIG. 19. Power spectral densities of pressure fluctuations at different circumferential probe locations inside the bi-swirl injector with various recess lengths.

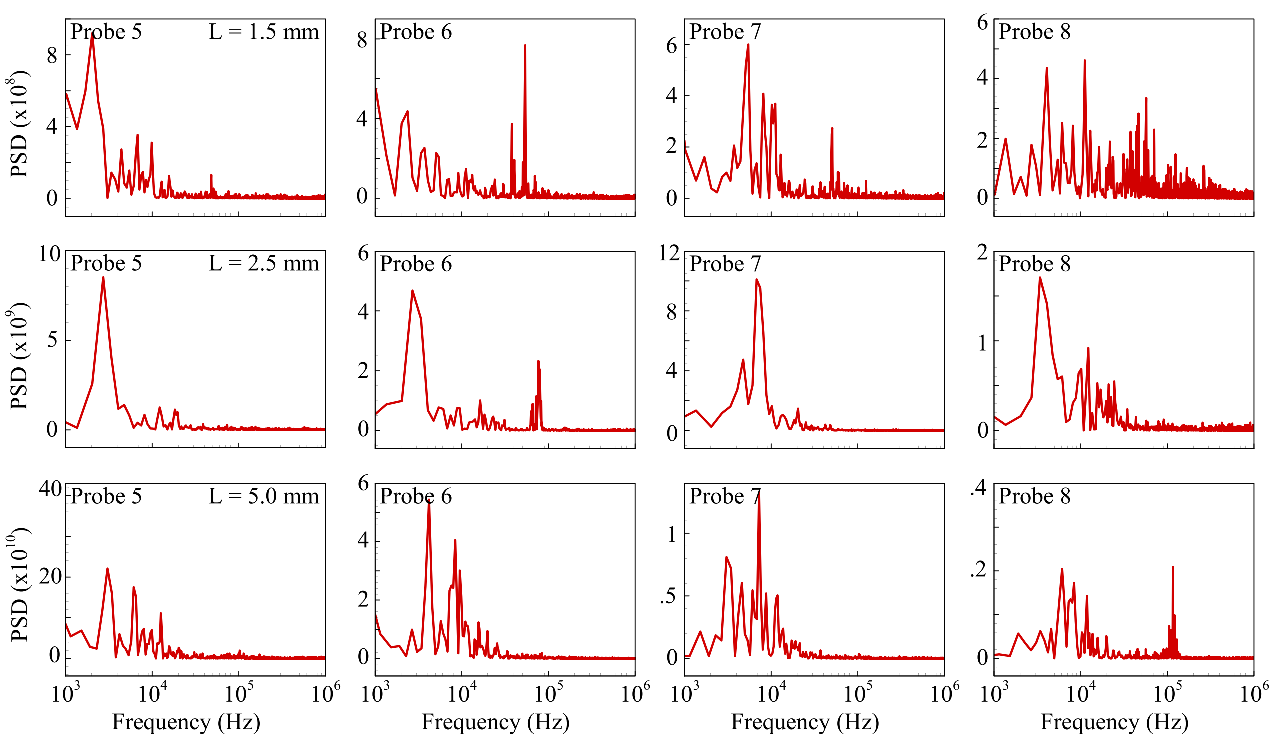

FIG. 20. Power spectral densities of pressure fluctuations at different longitudinal probe locations inside the bi-swirl injector with various recess lengths.

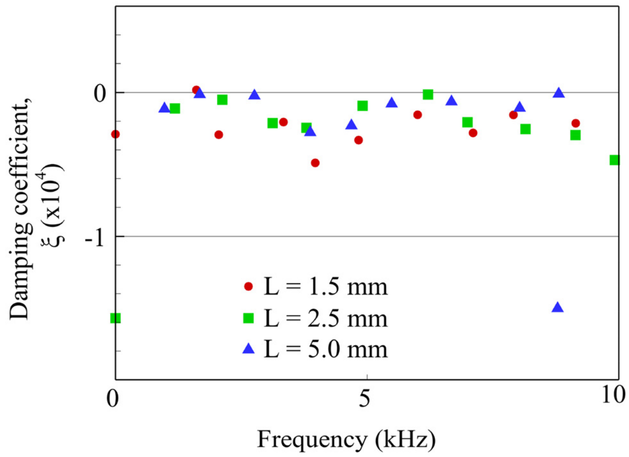

FIG. 21. Damping coefficient vs frequency obtained from DMD analysis on the x–y longitudinal cross section.

recess length of L = 1.5 mm, probe 7 exhibits a peak value at the frequency of 5.1 kHz, and probe 8 shows a slightly higher peak at 10 kHz. The lowest peak is for probe 5, which is 2 kHz. The values of PSD decrease away from the injector exit. For a recess length of L = 2.5 mm, probes 5 and 6 show a peak at around 2.9 kHz. At probe 7, a high peak at 7 kHz is observed. The location is just before the exit of the inner injector element. At probe 8, the peak value settles around 3.1 kHz. For a recess length of L = 5.0 mm, due to the internal mixing, the pressure spikes vary along the recess region of the inner injector element. Across all instances, the peak PSD and corresponding frequency decrease away from the injector exit. Moreover, an increase in PSD values is evident with an increase in the recess length of the injector. High-frequency pressure oscillations tend to diminish toward the injector exit, being replaced by a low-frequency mode.

H. Dynamic mode decomposition (DMD) analysis

The DMD is a powerful technique for extracting valuable information from a theoretical matrix, denoted as A, based on either experimental or computational data. The DMD used in this study employs the singular value decomposition (SVD) and the entire algorithm is given by Jourdain *et al.*[26] The resonant frequency, f_i, and the damping coefficient, ξ_i, for the ith extracted resonant mode can be calculated using specific parameters. These calculations are based on the time step, Δt, the number of time steps between two snapshots (N_{step}), and the corresponding eigenvalue (λ_i). The following equations describe the determination of these acoustic parameters:

$$\mathrm{Arg}(\lambda_i) = 2\pi f_i N_{step}\Delta t + 2\pi p, \tag{2}$$

$$\xi_i = \frac{\ln|\lambda_i|}{N_{step}\Delta t}. \tag{3}$$

The damping coefficient, ξ_i, provides crucial information about the stability characteristics of a specific resonant mode. If ξ_i is negative, then the amplitude of this mode will progressively decay or attenuate over time. Conversely, a positive ξ_i suggests that the amplitude of the mode will increase or amplify as time progresses. Furthermore, the damping coefficient allows for the evaluation of acoustic damping as a single, representative value across the entire chamber domain. This offers the advantage of a global parameter, in contrast to the localized damping factor.

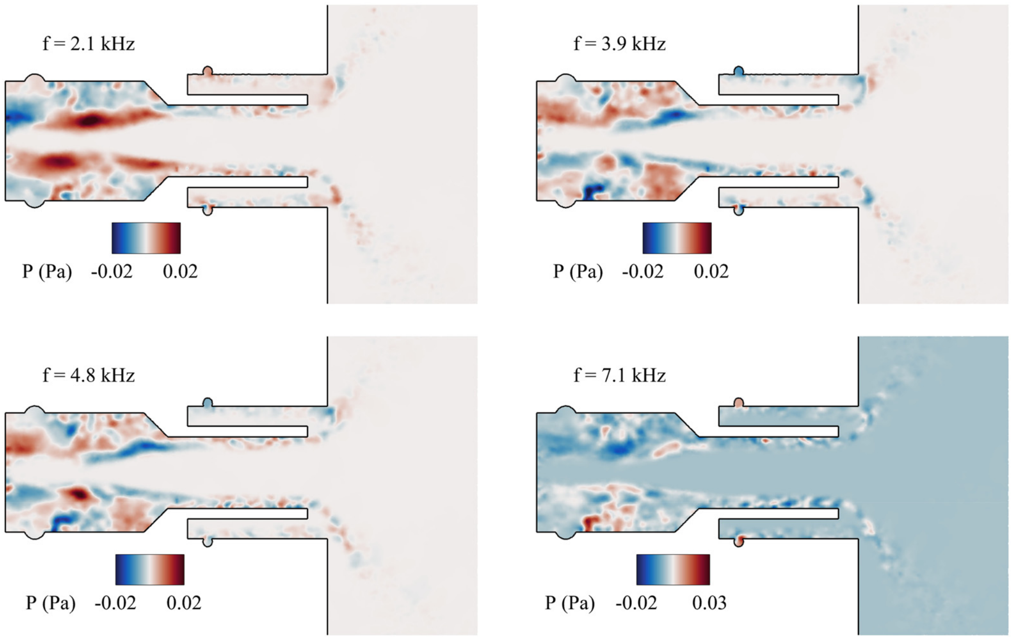

FIG. 22. DMD mode shapes of the bi-swirl injector with recess length of L = 1.5 mm.

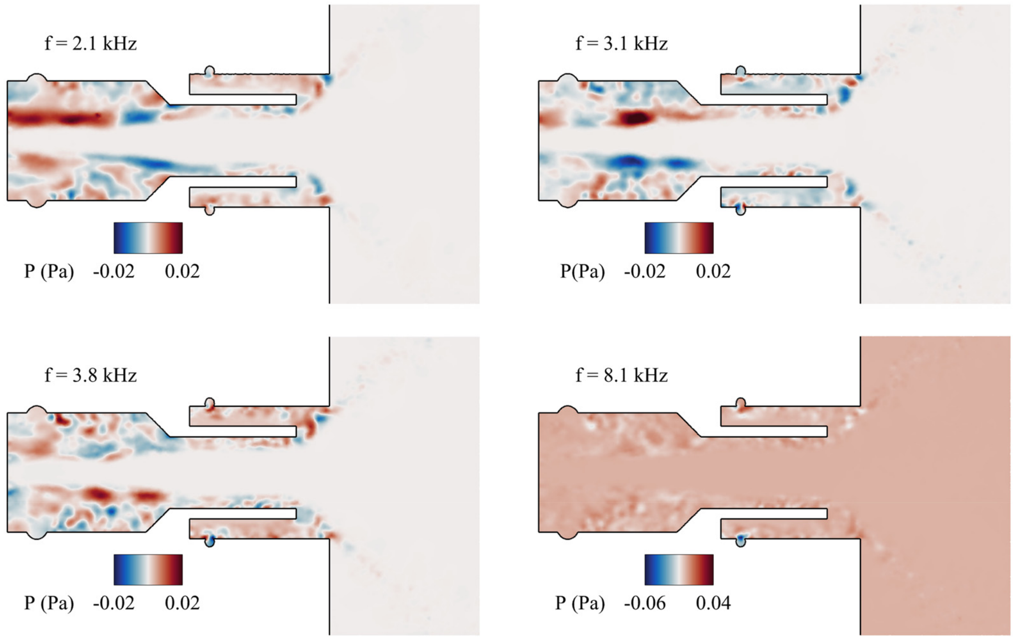

FIG. 23. DMD mode shapes of the bi-swirl injector with recess length of L = 2.5 mm.

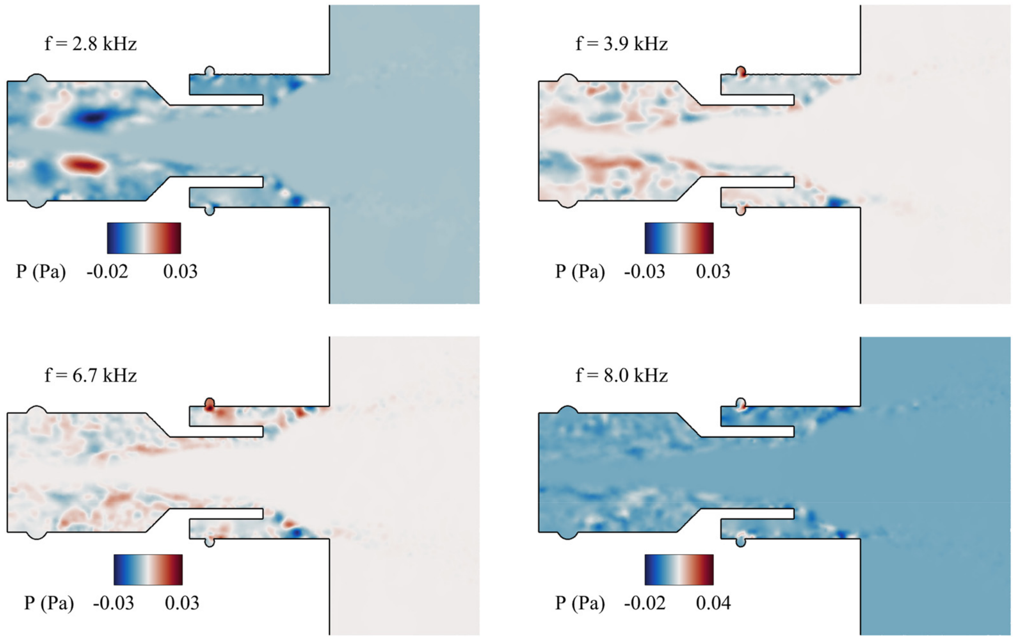

FIG. 24. DMD mode shapes of the bi-swirl injector cut section with recess length of L = 5.0 mm.

The implementation of the DMD technique in examining the flow dynamics has necessitated a careful selection of the time interval for snapshot collection. The sampling time of 10 μs is carefully selected to enable a comprehensive analysis of the flow dynamics with appropriate resolution since significant pressure fluctuations occur in the frequency range of 1–10 kHz based on the spectral analysis result. A recording time of 1 ms is set to enable the capturing of 101 snapshots between the time interval of 9–10 ms. This specific timeframe is chosen to efficiently record the range of frequencies essential for the analysis while optimizing computational resources. DMD analysis was conducted on two distinct

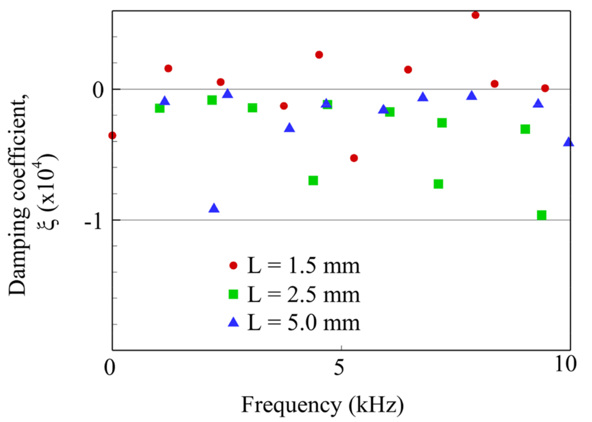

FIG. 25. Damping coefficient vs frequency obtained from DMD analysis on y–z transverse cross section at injector exit.

planes within the bi-swirl injector. The first plane comprises a longitudinal section, while the second plane is located at the injector exit, allowing for a comprehensive assessment of the injector flow characteristics.

Figure 21 shows the relationship between the damping coefficients and frequencies. All computed coefficients are found to be negative, suggesting a continuous decay in the amplitudes of various modes. The mode shapes for various frequencies, aligned with those derived from spectral analysis, are presented. These mode shapes represent the spatial patterns of flow structures at identified frequencies. By analyzing these mode shapes, we can understand how different flow structures interact and evolve over time. Each mode shape corresponds to a specific pattern of flow behavior, characterized by its frequency and growth/decay rate. By examining these mode shapes, the specific patterns of turbulence, vortex formation, or other dynamic phenomena could be identified and analyzed. Figure 22 shows the mode shapes of the swirl injector with a recess length of L = 1.5 mm. For frequencies of 2.1, 3.9, 4.8, and 7.1 kHz, the corresponding damping coefficients are −2937, −4905, −3312, and −2812, respectively. These values signify the decay of all modes over time. Similar mode shapes and corresponding damping coefficients are presented in Figs. 23 and 24 for different recess lengths of L = 2.5 and 5.0 mm, respectively. For the recess length of L = 2.5 mm, the damping coefficients for the frequencies 2.1, 3.1, 3.8, and 8.1 kHz are −506, −2137, −2458, and −2548, respectively. For the recess length of L = 5.0 mm, the damping coefficients for the frequencies 2.8, 3.9, 6.7, and 8.0 kHz are −231, −2788, −648, and −1084, respectively.

Figure 25 shows The DMD analysis conducted on the transverse plane at the injector exit, Unlike the situation on the longitudinal plane (Fig. 20), the analysis presented some positive damping coefficients for all recess lengths, indicating the presence of unstable modes. The phenomenon may be attributed to surface disturbances on the liquid film, which contribute to the amplification of wave motion and foster the process of liquid sheet breakup. Figure 26 shows the DMD mode shapes for a recess length of 1.5 mm. The damping coefficients for the frequencies 3.7 and 5.3 kHz have negative values of −1282 and −5291,

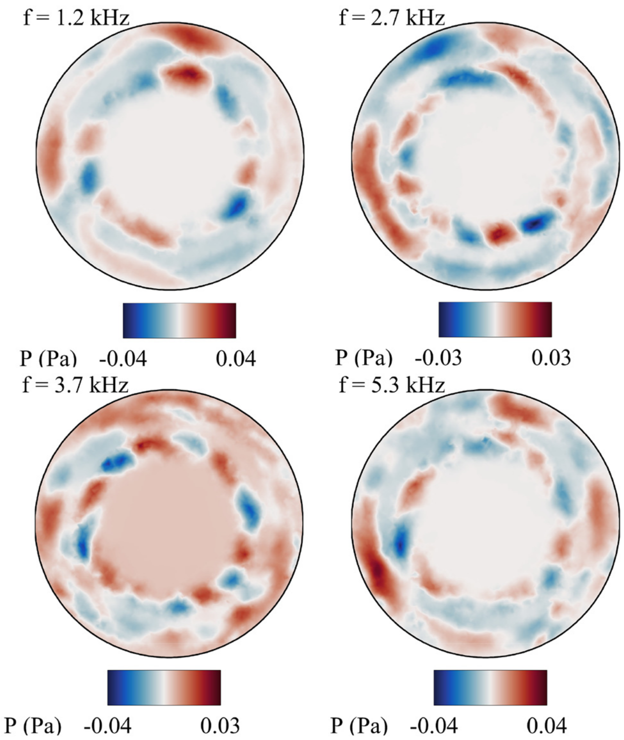

FIG. 26. DMD mode shapes of the bi-swirl injector exit plane with L = 1.5 mm.

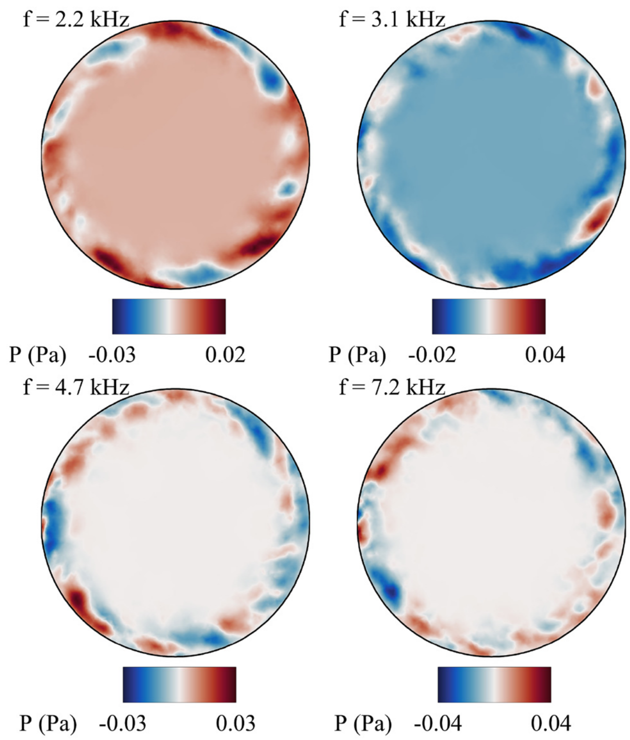

FIG. 27. DMD mode shapes of the bi-swirl injector exit plane with L = 2.5 mm.

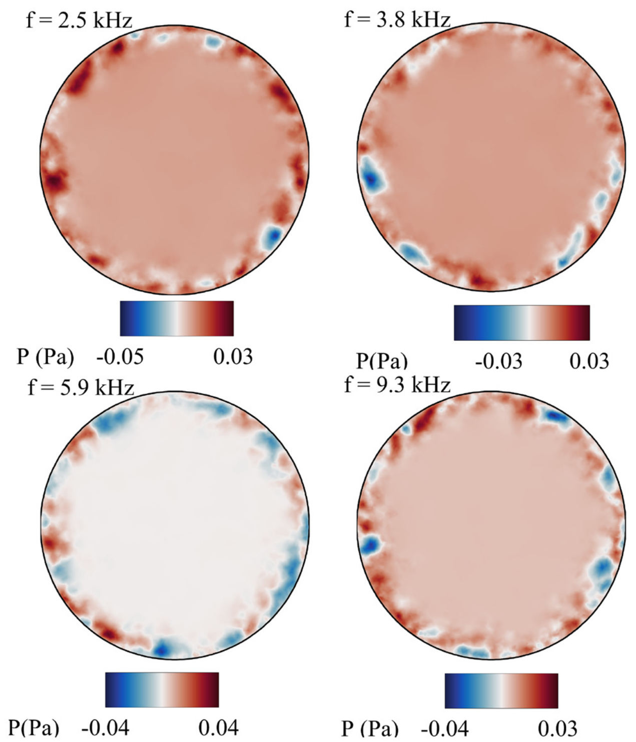

FIG. 28. DMD mode shapes of the bi-swirl injector exit plane with L = 5.0 mm.

respectively. These two modes are stable and decay with time. The other two modes are unstable and their amplitudes grow with time. The damping coefficients for the frequencies of 1.2 and 2.4 kHz are 1570 and 552, respectively. Figure 27 shows the DMD mode shapes for a recess length of 2.5 mm. All four modes are stable whose damping coefficients are −822, −1424, −1175, and −2576 for frequencies of 2.2, 3.1, 4.7, and 7.2 kHz, respectively. Figure 28 shows the DMD mode shapes for a recess length of 5.0 mm. In this case, all the modes are stable whose damping coefficients are −411, −3026, −1619, and −1162 for frequencies of 2.5, 3.8, 5.9, and 9.3 kHz, respectively. The mode shapes also illustrate the fuel and oxidizer flow positioning at the injector exit plane. For the recess length of L = 5.0 mm, the flow remains attached to the injector wall, in contrast to the situations with the recess lengths of L = 1.5 and 2.5 mm, where the flow is detached from the injector wall.

IV. CONCLUDING REMARKS

The present study deals with the flow dynamics and mixing of liquid–liquid bi-swirl injectors. The baseline configuration mimics the injector used in an operational liquid rocket engine RD-0110. Nonvolatile liquid oxygen (LOX) and kerosene are delivered into the injector initially filled with air. The analysis employs a validated multiphase solver in the OpenFOAM software, which solves three-dimensional conservation equations for the gas and liquid phases simultaneously. Turbulence closure is achieved by means of a large-eddy-simulation technique. A grid-independence study is conducted to determine the optimal grid resolution.

The fuel and oxidizer flowfields are examined systematically for injectors with different recess lengths of the inner injector element. Special attention is given to the evolution of liquid streams and their ensuing sprays downstream of the injector elements. Three different modes of mixing (i.e., internal, tip, and external) are observed, depending on the recess length of the inner injector element. A helical flow pattern and a wavy liquid film are observed within the injector. As recess length increases, the void region in the outer injector and overall spray cone angle decrease, along with a reduction in the liquid film thickness at the injector exit. The resultant spray for internal mixing becomes narrow, concentrated, and extends further downstream. Streamlines are obtained to shed light on the flow evolution within the injector. Vorticity dynamics are further explored along with spectral and DMD analyses, offering detailed insights into the underlying flow dynamics. Results from this study provide valuable information for optimizing similar types of injector designs for liquid-fueled propulsion systems.

ACKNOWLEDGMENTS

The present work was supported by the Space Launch Vehicle and Space Transportation Education and Research Center (NRF-2022M1A3C2076724) through the National Research Foundation (NRF) of Korea, funded by the Ministry of Science and ICT (MSIT) of the Republic of Korea Government.

AUTHOR DECLARATIONS

Conflict of Interest

The authors have no conflicts to disclose.

Author Contributions

Vishnu Natarajan: Data curation (equal); Formal analysis (equal); Investigation (equal); Methodology (equal); Software (equal); Validation (equal); Visualization (equal); Writing – original draft (equal). **Umesh Unnikrishnan:** Formal analysis (supporting); Investigation (supporting); Visualization (supporting); Writing – review & editing (supporting). **Jeong-Yeol Choi:** Conceptualization (equal); Data curation (equal); Funding acquisition (lead); Investigation (equal); Methodology (equal); Project administration (lead); Supervision (lead); Visualization (equal); Writing – review & editing (equal). **Vigor Yang:** Investigation (supporting); Supervision (equal); Visualization (supporting); Writing – review & editing (equal).

DATA AVAILABILITY

The data that support the findings of this study are available from the corresponding author upon reasonable request.

REFERENCES

[1]V. Bazarov, V. Yang, and P. Puri, *Design and Dynamics of Jet and Swirl Injectors* (American Institute of Aeronautics and Astronautics, 2004).
[2]V. G. Bazarov and V. Yang, "Liquid-propellant rocket engine injector dynamics," J. Propul. Power **14**, 797 (1998).
[3]V. Yang and W. E. Anderson, *Liquid Rocket Engine Combustion Instability* (AIAA Progress in Astronautics and Aeronautics, 1995).
[4]V. Yang, M. Habiballah, J. Hulka, and M. Popp, *Liquid Rocket Thrust Chambers: Aspects of Modeling, Analysis, and Design* (AIAA Progress in Astronautics and Aeronautics, 2004).

[5]L. Bayvel and Z. Orzechowski, *Liquid Atomization* (Taylor & Francis, Washington, DC, 1993).
[6]D. Kim, P. Han, J.-H. Im, Y. Yoon, and V. G. Bazarov, "Effect of recess on the spray characteristics of liquid-liquid swirl coaxial injectors," J. Propul. Power **23**, 1194 (2007).
[7]D. Sivakumar and B. N. Raghunandan, "Role of geometric parameters on the drop size characteristics of liquid-liquid coaxial swirl atomizers," At. Sprays **8**, 547 (1998).
[8]D. Sivakumar and B. N. Raghunandan, "Hysteretic interaction of conical liquid sheets from coaxial atomizers: Influence on the spray characteristics," Phys. Fluids **10**, 1384 (1998).
[9]D. Sivakumar and B. N. Raghunandan, "Formation and separation of merged liquid sheets developed from the mixing of coaxial swirling liquid sheets," Phys. Fluids **15**, 3443 (2003).
[10]V. R. Rubinsky, *Instability Phenomenology and Case Studies: Combustion Instability in the RD-0110 Engine*, Progress in Astronautics and Aeronautics (AIAA, 1995).
[11]X. Wang, H. Huo, Y. Wang, and V. Yang, "Comprehensive study of cryogenic fluid dynamics of swirl injectors at supercritical conditions," AIAA J. **55**, 3109 (2017).
[12]V. Natarajan, U. Unnikrishnan, W.-S. Hwang, J.-Y. Choi, and V. Yang, "Numerical study of two-phase flow dynamics and atomization in an open-type liquid swirl injector," Int. J. Multiphase Flow **143**, 103702 (2021).
[13]G. Taylor, "The mechanics of swirl atomizers," in Seventh International Congress of Applied Mechanics Vol. 2 (1948), pp. 280–285.
[14]G. N. Abramovich, *The Theory of Swirl Atomizers* (Industrial Aerodynamics, BNT ZAGI, Moscow, Russia, 1944).
[15]P.-G. Han, J.-H. Seol, S.-H. Hwang, and Y. Yoon, *The Spray Characteristics of Swirl Coaxial Injectors* (American Institute of Aeronautics and Astronautics, 2003).
[16]W. Yoon and K. Ahn, "Experimental and theoretical study on spray angles of bi-swirl coaxial injectors," J. Appl. Fluid Mech. **11**, 1377 (2018).
[17]B. Lee, W. Yoon, and K. Ahn, "A CFD study on the spray characteristics of bi-swirl coaxial injectors," in Proceedings of ILASS - Korea Annual Meeting, Jeju, Korea, 2017.
[18]X. Wang, Y. Wang, and V. Yang, "Geometric effects on liquid oxygen/kerosene bi-swirl injector flow dynamics at supercritical conditions," AIAA J. **55**, 3467 (2017).
[19]X. Wang, Y. Li, Y. Wang, and V. Yang, "Near-field flame dynamics of liquid oxygen/kerosene bi-swirl injectors at supercritical conditions," Combust. Flame **190**, 1 (2018).
[20]X. Wang and V. Yang, "Supercritical mixing and combustion of liquid-oxygen/kerosene bi-swirl injectors," J. Propul. Power **33**, 316 (2017).
[21]J.-W. Ding, G.-X. Li, and Y.-S. Yu, "Numerical investigation on liquid sheets interaction characteristics of liquid-liquid coaxial swirling jets in bipropellant thruster," Int. J. Heat Fluid Flow **62**, 129 (2016).
[22]L. Huang, S. Deng, J. Guan, W. Hua, and M. Chen, "Separation performance of a novel liquid–liquid dynamic hydrocyclone," Ind. Eng. Chem. Res. **57**, 7613 (2018).
[23]A. Motin and A. Bénard, "Design of liquid–liquid separation hydrocyclones using parabolic and hyperbolic swirl chambers for efficiency enhancement," Chem. Eng. Res. Des. **122**, 184 (2017).
[24]H. Osei, H. H. Al-Kayiem, and A. B. Osman, "Flow dynamics behaviour of a novel liquid-liquid hydrocyclone with varying upper cylindrical lengths and number of inlets," J. Eng. Appl. Sci. **11**, 12159 (2016).
[25]G. E. Cossali, M. Marengo, A. Coghe, and S. Zhdanov, "The role of time in single drop splash on thin film," Exp. Fluids **36**, 888 (2004).
[26]G. Jourdain, L.-E. Eriksson, S. H. Kim, and C. H. Sohn, "Application of dynamic mode decomposition to acoustic-modes identification and damping in a 3-dimensional chamber with baffled injectors," J. Sound Vib. **332**, 4308 (2013).